PAPER

Magnetic-field-induced deformation and spin-resolved flat-band localization in a Lieb lattice

Journal of Physics: Condensed Matter

PAPER

RECEIVED
9 November 2025

REVISED
25 January 2026

ACCEPTED FOR PUBLICATION
9 March 2026

PUBLISHED
2 April 2026

Magnetic-field-induced deformation and spin-resolved flat-band localization in a Lieb lattice

Nana Chang[1] **and Xiaoji Zhou**[1,2,*]

[1] State Key Laboratory of Photonics and Communications, School of Electronics, Peking University, Beijing 100871, People's Republic of China
[2] Institute of Carbon-based Thin Film Electronics, Peking University, Shanxi, Taiyuan 030012, People's Republic of China
[*] Author to whom any correspondence should be addressed.

E-mail: xjzhou@pku.edu.cn and nnchangqq@gmail.com

Keywords: flat band, localization, Aharonov–Bohm caging, Lieb lattice, synthetic gauge field

Abstract

We investigate the magnetic-field-induced deformation of electronic bands in the Lieb lattice within a tight-binding framework, focusing on the interplay between Aharonov–Bohm (AB) caging and Zeeman splitting. By incorporating Peierls phases and Zeeman effects, we demonstrate that magnetic flux can modulate the degeneracy and bandwidth of flat bands, leading to spin-resolved localization phenomena. Specifically, at a perpendicular flux of $\phi = \pi$, AB caging localizes particles into flat-band states, while Zeeman coupling lifts spin degeneracy and induces spin-selective energy shifts. This stabilization of flat bands facilitates tunable, spin-selective transport and magnetic responses. Our findings position the Lieb lattice as a versatile platform for quantum simulation and spin-resolved control, with potential applications in synthetic systems such as ultracold atoms, photonic lattices, and superconducting circuits. These results offer insights into the controlled engineering of spin-resolved localization and flat-band physics, providing a pathway for future experiments and applications in quantum materials.

1. Introduction

The Lieb lattice, experimentally realized in ultracold atomic lattices [1], photonic waveguide arrays [2], Rydberg lattices [3], and programmable quantum circuits [4], has long served as a paradigmatic model for exploring geometric frustration and localization in condensed matter systems, which features a perfectly dispersionless flat band intersecting dispersive bands at a Dirac-like point [5–7]. Its intrinsic flat band at zero energy arises purely from lattice interference rather than from interactions [6–13], where the vanishing kinetic energy enhances interaction effects, making them fertile ground for realizing exotic quantum states. Owing to destructive interference, it hosts a perfectly flat band at zero energy in the absence of external perturbations, making it an ideal platform for studying exotic quantum states.

Experimental realizations span ultracold atomic setups [1, 14, 15], photonic lattices [16], polariton lattices [17], and superconducting circuits [4], making it an ideal platform for studying compact localized states, Aharonov–Bohm (AB) caging, and flat-band related phenomena such as magnetism, superconductivity, and topological transport [14, 16, 18–24]. Owing to destructive interference, it hosts a perfectly flat band at zero energy in the absence of external perturbations, making it an ideal platform for studying exotic quantum states. Experimental realizations span ultracold atomic setups [1, 14], photonic lattices [16], polariton lattices [17], and superconducting circuits [4].

Similar to how thermal fluctuations modify Bloch oscillations in atomic systems [25], magnetic fields can induce nontrivial band deformations in lattices, i.e. applying a perpendicular magnetic field to the Lieb lattice modifies its band structure through two distinct mechanisms. The first is the orbital effect, in which Peierls phases alter hopping amplitudes [21, 22]. At a magnetic flux of $\phi = \pi$ per plaquette, destructive interference leads to the AB caging effect [2, 23, 26–32], where all eigenstates become strictly localized and the spectrum collapses into dispersionless bands. This effect has been observed in photonic

[16, 24], polaritonic, and ultracold-atom lattices. Note that for AB caging, in specific flux configurations, quantum interference can confine particles to localized regions, resulting in completely flat bands. This 'caging' phenomenon has profound implications for quantum transport, localization–delocalization transitions, and correlated many-body states. The second is Zeeman effect [33–41], whereby the magnetic field couples to the spin degree of freedom, lifting spin degeneracy and inducing spin-resolved shifts in the band dispersion. Note that Zeeman splitting, i.e. Spin-magnetic field coupling, introduces an additional degree of band deformation, lifting degeneracies and enabling spin-resolved control of energy spectra.

While the interplay between geometry and magnetic flux has been extensively investigated, the influence of spin degrees of freedom and Zeeman splitting remains less explored. In realistic systems, magnetic fields not only introduce Peierls phases but also induce Zeeman energy shifts, lifting the spin degeneracy of the energy levels. This spin-dependent energy shift leads to spin-selective band deformation, where spin-up and spin-down components experience distinct band reshaping and localization. Understanding this interplay between Zeeman splitting and AB caging is crucial for engineering spin-resolved flat bands and exploring spin-polarized transport phenomena in synthetic quantum systems.

In this work, we present a systematic study of magnetic field induced band deformation in the Lieb lattice by simultaneously incorporating orbital Peierls phases and Zeeman spin splitting. section 2 outlines a detailed proposal for realizing a Lieb lattice in ultracold atom systems. The evolution of the band structure in the absence of a magnetic field is analyzed in section 3, whereas the corresponding behavior in the presence of a magnetic field is discussed in section 4. The density of states (DOS) as a function of magnetic flux ϕ and Zeeman field B_z is presented in section 5, with particular emphasis on the regimes $\phi = 0$ and $\phi = \pi$, where AB caging leads to pronounced flatness, and on its deformation under varying Zeeman splitting. The corresponding analysis of the physical discussion for magnetic field induced band deformation in a Lieb lattice is illustrated in section 6.

Furthermore, section 7 discusses the standard high-symmetry path in the two-dimensional Brillouin zone of Lieb lattice. By computing DOS evolution across Zeeman fields, we reveal how the interplay between gauge-induced localization and spin polarization drives band restructuring and energetic asymmetry, which are relevant to current efforts in synthetic quantum systems, including cold atoms in optical lattices [1, 42], topological photonic lattices [14, 32], and superconducting circuit arrays [4]. Our results provide guiding principles for engineering tunable flat-band phenomena through combined magnetic control and spin manipulation. In addition, the conclusion holds in the section 8.

2. Engineering a Lieb lattice in ultracold atom systems

We consider noninteracting ultracold atoms loaded into a two-dimensional optical Lieb lattice, as illustrated in figure 1. The lattice can be generated by superimposing three standing-wave laser fields along orthogonal directions [1], forming three inequivalent sites A, B, and C per unit cell. At zero magnetic field, the tight-binding model features nearest-neighbor tunneling of amplitude t, yielding two dispersive bands intersected by a dispersionless flat band at zero energy, resulting from destructive interference among the sublattices.

Lattices are created by interfering laser beams to form periodic potentials that trap ultracold atoms. For example, Lieb and kagome lattices have been used to create flat bands with minimal dispersion [14, 15, 43–45]. These lattices can be tuned by adjusting the laser intensity and phase, allowing for the observation of localization phenomena. Atoms (like ^{6}Li, ^{87}Rb) are cooled to near absolute zero using magneto-optical traps and transferred into the optical lattice. One can observe band occupation and momentum distribution, explore quantum dynamics, e.g. quenching or time evolution, even probe topological properties, especially when synthetic gauge fields are introduced.

The combination produces a lattice geometry featuring three sites per unit cell (A, B, and C) of a Lieb lattice, showing the engineering process and the sketch in figures 1(a) and (b), respectively. The superlattice term introduces additional potential minima at the plaquette centers, allowing for control of site-specific energies and tunnelings. The realization of a uniform synthetic magnetic flux and the observation of AB caging in photonic lattices have been investigated theoretically [9, 46, 47] and experimentally [2, 7, 32]. The optical potential used to realize the Lieb lattice geometry is constructed by superimposing a primary square lattice with a longer-period superlattice. The resulting potential landscape is given by

$$V(x,y) = -V_s\left[\cos^2(kx) + \cos^2(ky)\right] - V_p\cos^2\left(\frac{kx}{2}\right)\cos^2\left(\frac{ky}{2}\right), \tag{1}$$

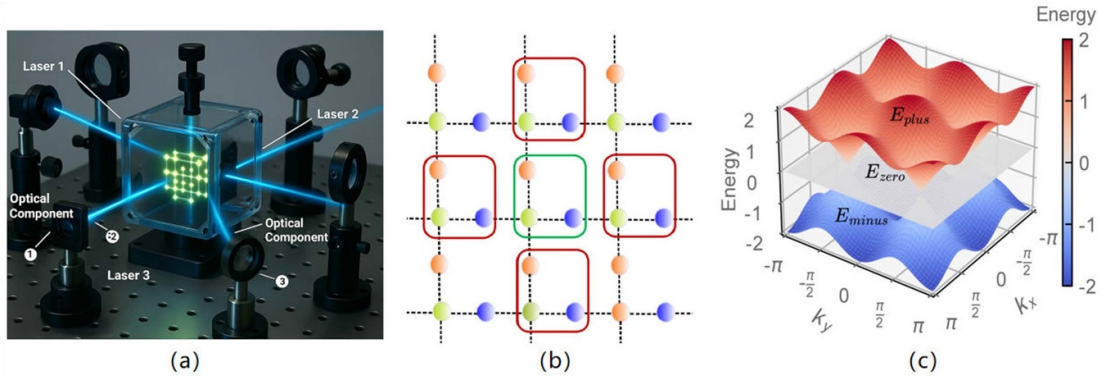

Figure 1. Schematic illustration of the engineered Lieb lattice and its intrinsic band geometry. (a) Ultracold atoms (e.g. ^{6}Li, ^{87}Rb) are laser-cooled and confined in a two-dimensional optical lattice generated by three standing-wave laser beams. (b) The resulting Lieb lattice consists of three sublattices A (orange), B (green), and C (purple), forming a square-depleted geometry that supports a characteristic flat band at zero energy.(c) The corresponding tight-binding band structure in the absence of external fields exhibits a dispersionless flat band between two dispersive ones, serving as the basis for magnetic-field engineering of spin-selective band deformation and Aharonov–Bohm caging.

where V_s denotes the depth of the primary square lattice, and V_p represents the strength of the superlattice modulation. The wave vector $k = 2\pi/\lambda$ corresponds to the wavelength λ of the laser beams.

Experimental realizations of artificial magnetic fields with ultracold atoms have been achieved in optical lattices, where laser-assisted tunneling in tilted potentials generates spatially dependent complex tunneling amplitudes. In such systems, atoms accumulate phase shifts equivalent to the AB phase, enabling the direct implementation of the Hofstadter Hamiltonian and the observation of cyclotron orbits [48, 49]. Furthermore, using two atomic spin states with opposite magnetic moments, these setups naturally realize a time-reversal-symmetric Hamiltonian, providing a cold-atom platform for exploring the quantum spin Hall effect [50–52]. Using scanning tunneling microscopy imaging, wave-function mapping, and spectroscopy, the team directly probed the electronic structure, confirming hallmark features of the Lieb lattice: Dirac cones, flat bands, and higher-order super-Lieb patterns at elevated energies [53, 54].

As a result, the experimental schematic of a Lieb lattice implemented with ultracold atoms in an Lieb optical lattice under a synthetic magnetic field, which consists of a 3D optical lattice, is shown in figure 2. Note that an additional pair of laser beams (red arrows) with wave vectors $|\vec{k}_1| \approx |\vec{k}_2| = 2\pi/\lambda_K$ and frequency difference $\omega = \omega_1 - \omega_2 = \Delta/\hbar$ is to restore resonant tunneling with complex amplitude K. This realizes an effective flux $\phi = \pi/2$ for $|\uparrow\rangle$ atoms and $-\phi$ for $|\downarrow\rangle$ atoms in figures 2(a) and (b), respectively. Lieb lattice geometry features three inequivalent sites per unit cell. Complex hopping amplitudes are realized through laser-assisted tunneling, effectively generating a uniform artificial magnetic flux ϕ per plaquette. The Peierls phases imprinted on the tunneling paths give rise to magnetic effects analogous to those in the Hofstadter model.

3. Energy band in the absence of external field

Lieb lattice, a two-dimensional lattice with a specific arrangement of sites(corner sites(olive green), horizontal edge sites(purple), and vertical edge sites(orange)) can be described using a tight-binding model, which is shown in figure 1(b). The Hamiltonian for Lieb lattice in the absence of external fields is given by the tight-binding Hamiltonian in real space

$$H = -t\sum_{\langle i,j\rangle}\left(A_i^{\dagger}B_j + A_i^{\dagger}C_j + \text{h.c.}\right), \tag{2}$$

where $A_i^{\dagger}$, $B_j^{\dagger}$, $C_j^{\dagger}$ are creation operators on sublattices A, B, and C. The sum $\langle i,j\rangle$ runs over nearest neighbors.

Then, the tight-binding Hamiltonian for Lieb lattice in the momentum space can be written as

$$H(\mathbf{k}) = \epsilon_0\mathbf{I} + t\sum_{\delta} e^{i\mathbf{k}\cdot\delta}\mathbf{C}_{\delta}, \tag{3}$$

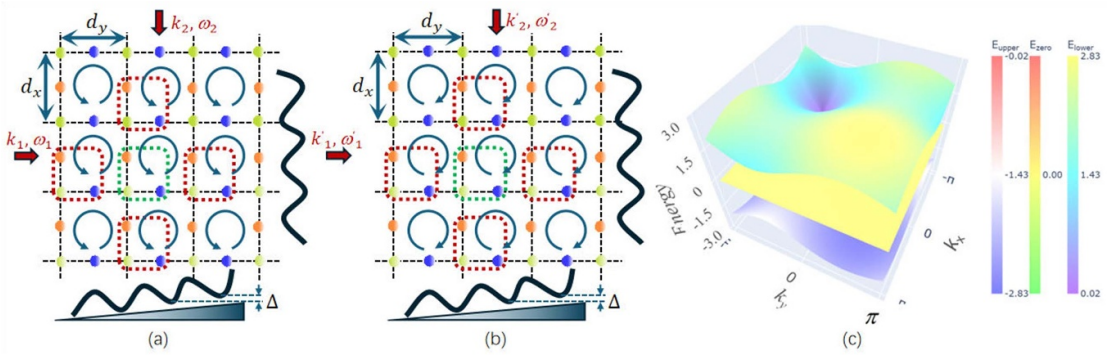

Figure 2. Experimental schematic for realizing a spin-resolved Lieb lattice with ultracold atoms in an optical lattice under a synthetic magnetic field. A three-dimensional optical lattice confines atoms such as ^{6}Li or ^{87}Rb, where the vertical lattice isolates individual two-dimensional planes. The lattice constants within each plane are $|\vec{d}_i| = \lambda_i/2$, where $i = x, y$. Along y, bare tunneling occurs with strength J, while tunneling along x is inhibited by a magnetic field gradient B', which introduces an energy offset between neighboring sites of (a) Δ for $|\uparrow\rangle$ atoms and (b) Δ for $|\downarrow\rangle$ atoms. Note that an additional pair of laser beams (red arrows) with wave vectors $|\vec{k}_1| \approx |\vec{k}_2| = 2\pi/\lambda_K$ and frequency difference $\omega = \omega_1 - \omega_2 = \Delta/\hbar$ is to restore resonant tunneling with complex amplitude K. This realizes an effective flux of (a) $\phi = \pi/2$ for $|\uparrow\rangle$ atoms and (b) ϕ for $|\downarrow\rangle$ atoms. The Lieb lattice geometry features three inequivalent sites per unit cell. Complex hopping amplitudes are realized through laser-assisted tunneling, effectively generating a uniform artificial magnetic flux ϕ per plaquette. For comparison, there hold the corresponding primed parameters (k'_1, ω'_1), (k'_2, ω'_2). (c) Energy bands for the Lieb lattice exposed in a magnetic field.

where ϵ_0 is the on-site energy, t is the hopping parameter, δ represents the nearest-neighbor vectors, $\mathbf{C}_\delta$ are the hopping matrices. The energy dispersion relation is

$$(E-\epsilon_0)^3 - t^2 e^{ik_x a} e^{-ik_x a}(E-\epsilon_0) - t^2 e^{ik_y a} e^{-ik_y a}(E-\epsilon_0) = 0. \tag{4}$$

In the absence of magnetic and DC fields, the flat band in the Lieb lattice is characterized by zero dispersion. The energy of the flat band is determined by the on-site energies and the hopping parameters. The flat band is highly degenerate, leading to enhanced electron–electron interactions and the emergence of strongly correlated states [55]. When $\epsilon_0 = 0$, the band structure for the Lieb lattice in the absence of any external field is as in figure 1(c). Due to the destructive interference of the electron wave functions at the corner and edge sites [7, 9, 11–13, 55, 56], flat band exists, characterized by a dispersionless energy band, where the energy remains constant regardless of the momentum of the particles. These lattices can be tuned by adjusting the laser intensity and phase, allowing for the observation of localization phenomena.

4. Energy band in the presence of a magnetic field

The tight-binding Hamiltonian for the Lieb lattice is constructed with nearest-neighbor hopping $t = 1$ and periodic boundary conditions on a 10 $\times$ 10 lattice. A perpendicular magnetic field introduces a Peierls phase in the hopping amplitudes, implemented as a complex exponential factor along the y-direction proportional to the flux ϕ per unit cell. The full Hamiltonian matrix of size 300 $\times$ 300 is diagonalized to obtain all eigenvalues, and the DOS is computed by histogramming these eigenvalues with 200 bins and proper normalization.

The DOS is computed by evaluating the spectrum of the tight-binding Hamiltonian and applying Gaussian broadening to approximate the delta functions. Specifically, the DOS is given by

$$D(E) = \frac{1}{N\sqrt{2\pi\sigma^2}} \sum_n \exp\left(-\frac{(E-E_n)^2}{2\sigma^2}\right), \tag{5}$$

where E_n are the eigenvalues of the Hamiltonian, N is the total number of eigenstates, and σ is the broadening parameter. In our calculations, we choose $\sigma = 0.05$, which provides a smooth approximation while preserving fine spectral features.

Figure 3 presents the magnetic-flux dependence of the DOS in the Lieb lattice. Figure 3(a) shows the overall evolution of the DOS as the magnetic flux ϕ varies from 0 to 2π. With increasing ϕ, the spectral weight redistributes and clear flattening of the bands emerges, signaling the onset of magnetic-field-induced localization. At the special flux $\phi = \pi$, as shown in (b), the system exhibits a sharp peak at

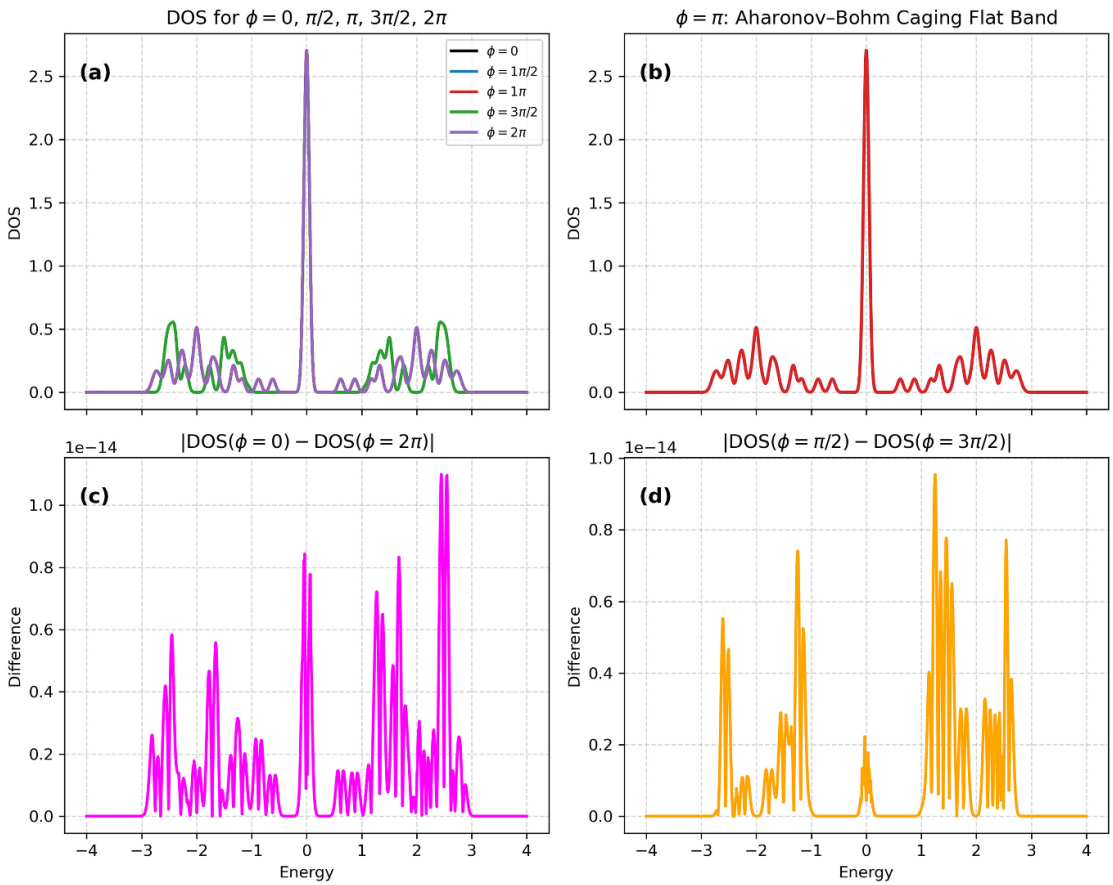

Figure 3. (a) Density of states (DOS) of the Lieb lattice under various magnetic flux values $\phi = 0$, $\pi/2$, π, $3\pi/2$, and 2π, illustrating the spectral evolution and the emergence of band flattening as the magnetic field increases. (b) The DOS at $\phi = \pi$, where Aharonov–Bohm caging induces a prominent flat band at zero energy. (c) Absolute difference between the DOS at $\phi = 0$ and 2π, confirming the recovery of magnetic periodicity. (d) Absolute difference between the DOS at $\phi = \pi/2$ and $3\pi/2$, highlighting the field-reversal symmetry around $\phi = \pi$. The data collectively demonstrate the π-periodic Aharonov–Bohm interference pattern and the associated flattening of energy bands in the Lieb lattice.

zero energy, reflecting the formation of an Aharonov–Bohm cage that traps the wave functions on local plaquettes.

In the presence of a uniform magnetic field, the effect of the flux is incorporated through the Peierls substitution, whereby each nearest-neighbor hopping acquires a phase factor such that the accumulated phase around an elementary plaquette equals the magnetic flux ϕ. In the Lieb lattice, the connectivity of the lattice allows multiple equivalent hopping paths between neighboring sites, whose quantum amplitudes interfere. At half a flux quantum per plaquette, $\phi = \pi$ the Peierls phases associated with these paths differ by a phase of π, resulting in complete destructive interference. Consequently, all momentum-dependent hopping terms cancel exactly in the Bloch Hamiltonian. The resulting Hamiltonian becomes independent of the crystal momentum, and all energy bands collapse into perfectly flat bands. This complete band flattening suppresses wave-packet dispersion and leads to strict localization of eigenstates within a finite cluster of lattice sites, a phenomenon known as AB caging. For flux values different from $\phi = \pi$, the destructive interference is incomplete, the momentum dependence is restored, and the bands acquire a finite dispersion, lifting the caging effect.

To verify the periodicity of the magnetic response, figure 3(c) compares the DOS at $\phi = 0$ and 2π, showing that their difference nearly vanishes, consistent with the 2π periodicity of the Peierls phase. Finally, panel (d) contrasts the DOS between $\phi = \pi/2$ and $3\pi/2$, demonstrating a clear field-reversal symmetry about $\phi = \pi$. Together, these results visualize the π-periodic band deformation and the emergence of flat bands associated with the Aharonov–Bohm caging effect.

Upon introducing a synthetic magnetic flux and Zeeman field, the system evolves into a spin-resolved configuration as shown in figure 2. A magnetic-field gradient B' induces spin-dependent on-site offsets Δ_σ through Zeeman splitting, while two Raman beams restore resonant tunneling with complex

amplitude $Ke^{i\phi_\sigma}$, generating an effective flux ϕ_σ per plaquette. This setup enables independent control of $\phi_\uparrow$ and $\phi_\downarrow$, resulting in spin-dependent Peierls phases and tunable Zeeman shifts.

Such synthetic gauge fields have been experimentally realized via laser-assisted tunneling in tilted optical lattices [48, 49]. Atoms accumulate AB phases equivalent to a magnetic flux, effectively implementing the Hofstadter Hamiltonian. Using two spin states with opposite magnetic moments naturally realizes a time-reversal-symmetric configuration, paving the way for spin-resolved AB caging and flat-band engineering in synthetic quantum systems [7, 57]. We consider a tight-binding Hamiltonian on a two-dimensional Lieb lattice under the influence of both a uniform magnetic field and a Zeeman field. The system contains three sublattices per unit cell and is defined on a $L_x \times L_y$ square grid with periodic boundary conditions. The magnetic field is introduced via Peierls substitution, which assigns complex hopping phases according to the vector potential. For a magnetic flux ϕ per plaquette, the hopping along the A–C bonds acquires position-dependent Peierls phases $e^{\pm i2\pi\phi x/2\pi}$, while the A–B bonds remain unmodified. Including Zeeman effect as a spin-dependent onsite energy shift, the total Hamiltonian becomes spin-block-diagonal, i.e.

$$H_{\text{total}} = \begin{pmatrix} H_0 + B_z\mathbb{I} & 0 \\ 0 & H_0 - B_z\mathbb{I} \end{pmatrix}, \tag{6}$$

where H_0 is the spinless tight-binding Hamiltonian with magnetic flux, and B_z is the out-of-plane Zeeman field strength.

The DOS is computed by diagonalizing H_{total} and applying Gaussian broadening

$$D(E) = \frac{1}{\sqrt{2\pi}\sigma} \sum_n \exp\left[-\frac{(E - E_n)^2}{2\sigma^2}\right], \tag{7}$$

with $\sigma = 0.05$ and energy sampled over a grid $E \in [-4, 4]$.

5. Zeeman-induced spin splitting of DOS at $\phi = 0$ and $\phi = \pi$

To further characterize the influence of Zeeman splitting on the magnetic-field-induced localization, we calculate the DOS and the corresponding band flatness parameter η as shown in figure 4. At $\phi = \pi$ and $B_z = 0$, the flat band produces a pronounced delta-like DOS peak, reflecting the complete Aharonov–Bohm caging of wave functions. As the Zeeman field increases, this peak broadens and splits into two spin-resolved components, signaling the spin-selective breakdown of perfect localization. The quantitative flatness measure $\eta = W^{-1}$, defined as the inverse of the bandwidth W, decreases asymmetrically for the two spin branches, demonstrating that the interplay between Zeeman energy and Peierls phase deforms the originally dispersionless band in a controllable manner. Such spin-dependent flatness modulation offers a feasible route to engineer tunable localization and correlated phases in synthetic Lieb lattices.

The stark difference between the $\phi = 0$ and $\phi = \pi$ cases highlights the role of magnetic flux in shaping the spectral flatness and its sensitivity to Zeeman perturbations. The $\phi = \pi$ flat band is particularly susceptible to spin splitting due to its highly localized nature, while the $\phi = 0$ states respond more smoothly due to their dispersive character. These features are of interest for cold atom emulations of flat-band systems, as well as for exploring interaction effects in spin-split flat-band platforms.

6. Physical discussion

The application of a perpendicular magnetic flux ϕ threading each unit cell modifies the band structure through complex hopping phases introduced by the Peierls substitution. This results in the splitting of the energy bands into magnetic subbands, which can exhibit fractal-like patterns (e.g. Hofstadter butterfly) at rational values of the flux.

In Lieb lattice, the presence of magnetic field notably affects the flat band by inducing band splitting and opening of gaps. The interference between hopping paths due to the magnetic field alters localization properties and modifies the DOS. At $\phi = \pi$, these effects are especially pronounced, causing significant rearrangement of the energy levels and the formation of distinctive spectral features arising from the lattice symmetry and magnetic flux.

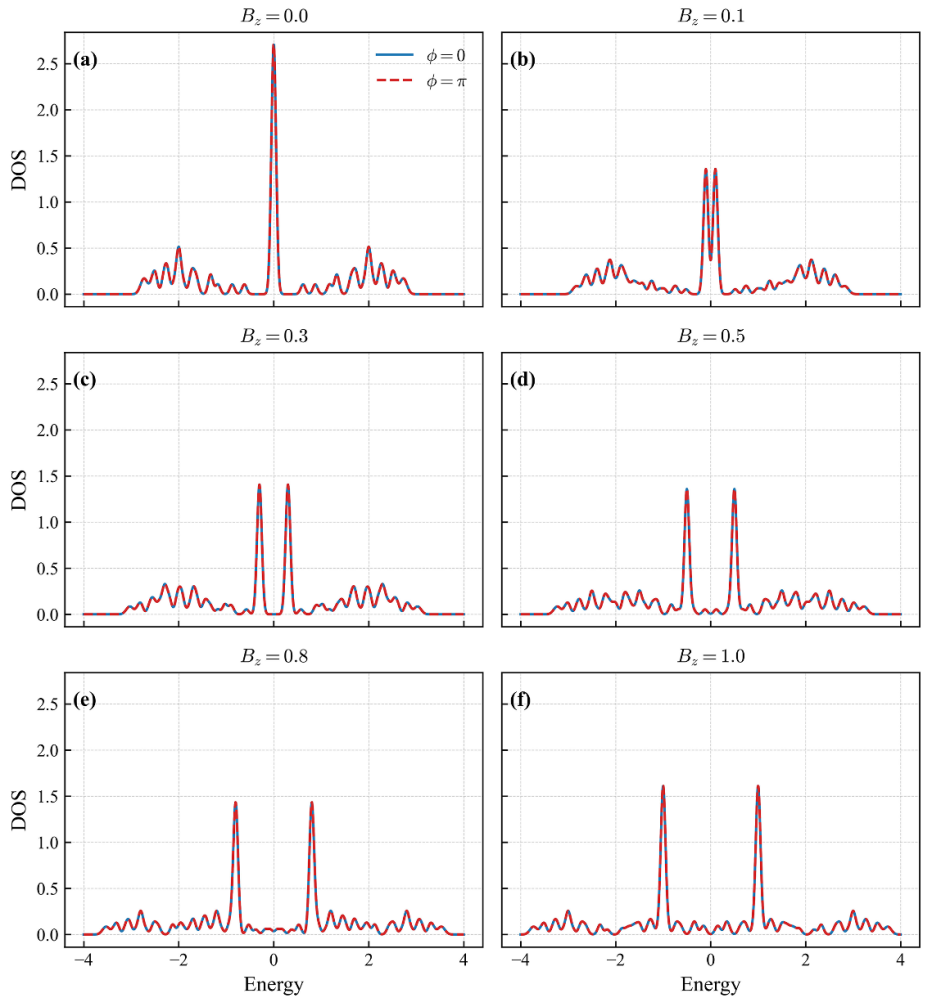

Figure 4. Evolution of the density of states (DOS) and band flatness in the Lieb lattice as functions of magnetic flux ϕ and Zeeman splitting B_z. (a)–(c) show the Gaussian-broadened DOS for different Zeeman strengths, where the sharp delta-like peak at $\phi = \pi$ gradually broadens and splits with increasing B_z, indicating the breakdown of perfect Aharonov–Bohm (AB) caging. (d) Quantitative flatness measure $\eta = W^{-1}$ (the inverse of the bandwidth W) reveals a spin-selective reduction of band flatness, highlighting the tunable localization-to-dispersion crossover driven by the interplay between Peierls phase and Zeeman energy.

6.1. AB effect

When a magnetic field is applied perpendicular to the Lieb lattice, the Hamiltonian is modified to include the vector potential **A**

$$H_B = -t \sum_{\langle i,j \rangle} \mathrm{e}^{\mathrm{i}\frac{e}{\hbar c}\int_i^j \mathbf{A}\cdot\mathrm{d}\mathbf{r}} \left(c_i^\dagger c_j + \mathrm{h.c.} \right) + \sum_i \epsilon_i c_i^\dagger c_i. \tag{8}$$

AB effect ($\phi = \pi$) profoundly influences electron motion in a Lieb lattice by inducing phase shifts that lead to destructive interference and electron localization [58].This effect, known as AB caging, results in perfectly flat bands in the energy spectrum. However, the presence of electron–electron interactions can disrupt this caging effect, leading to delocalization and changes in the electronic properties of lattice.

Thus, the Hamiltonian for the Lieb lattice with AB cage effect can be written as

$$H = \sum_{m,n} \left(t_{AB} \left(\mathrm{e}^{\mathrm{i}\theta_{m,n}} c_{A_{m,n}}^\dagger c_{B_{m,n}} + \mathrm{h.c.} \right) + t_{AC} \left(c_{A_{m,n}}^\dagger c_{C_{m,n}} + \mathrm{h.c.} \right) + t_{BC} \left(c_{B_{m,n}}^\dagger c_{C_{m,n}} + \mathrm{h.c.} \right) \right), \tag{9}$$

where t_{AB}, t_{AC}, and t_{BC} are the hopping parameters between different sites, $c^\dagger$ and c are the creation and annihilation operators, respectively, and $\theta_{m,n} = \alpha m$ represents the phase shift due to the magnetic field, with α being the magnetic flux through the unit cell. The Magnetic Field Strength, i.e. magnetic flux ϕ through each unit cell is given by $\phi = \alpha\phi_0$, where $\phi_0 = h/e$ is the flux quantum. For the AB cage effect to be significant, α is typically chosen to be $1/2$, corresponding to a flux of $\phi = \phi_0/2$.

To calculate the energy bands, we consider the tight-binding model in the momentum space. The Bloch Hamiltonian for the Lieb lattice with the AB cage effect can be written as

$$H(\mathbf{k}) = t_{AB}\left(\mathrm{e}^{\mathrm{i}(k_x+\alpha)}\sigma_x + \mathrm{e}^{-\mathrm{i}(k_x+\alpha)}\sigma_x\right) + t_{AC}\left(\mathrm{e}^{\mathrm{i}k_y}\sigma_y + \mathrm{e}^{-\mathrm{i}k_y}\sigma_y\right) + t_{BC}\left(\mathrm{e}^{\mathrm{i}k_x}\sigma_z + \mathrm{e}^{-\mathrm{i}k_x}\sigma_z\right), \tag{10}$$

where $(\mathbf{k} = (k_x, k_y))$ is the wave vector, and (σ_x), (σ_y), (σ_z) are the Pauli matrices. The energy bands are obtained by solving the eigenvalue problem $H(\mathbf{k})\psi = E(\mathbf{k})\psi$. For $\alpha = 1/2$(The ratio of the magnetic flux in each unit cell to 2π), the energy bands exhibit significant changes due to the AB cage effect. The flat band becomes completely flat, and the other bands show non-trivial dispersion. The energy bands can be plotted as a function of the wave vector $(\mathbf{k})$.

Thus, AB cage effect significantly alters the energy band structure of the Lieb lattice, leading to the complete flattening of the flat band and non-trivial dispersion of other bands, which introduces a phase shift in the electron wave functions, altering the interference patterns and, consequently, the energy levels of the flat band. In the Lieb lattice, the AB effect can lead to a dispersion of the flat band, meaning that the originally flat band can acquire a non-zero bandwidth. This dispersion arises because the phase shift depends on the electron's path and the magnetic flux through the loops formed by the lattice sites. The energy levels of the flat band can change and spread out, leading to a more complex band structure. This effect provides a unique platform for studying the interplay between magnetic fields and electronic states in two-dimensional lattices.

6.2. Zeeman splitting

The application of a magnetic field to the Lieb lattice can significantly affect the energy levels of the flat band through several key mechanisms: the Zeeman effect, AB effect, and modifications to the band structure. Zeeman effect arises because electrons have an intrinsic magnetic moment due to their spin. When a magnetic field is applied, this magnetic moment interacts with the field, causing the energy levels to split. This splitting is proportional to the strength of the magnetic field and the spin orientation of the electrons. This splitting lifts the degeneracy of the flat band and affects the overall energy structure,

$$H_Z = \frac{1}{2}g\mu_{\mathrm{B}}B\sum_i \sigma_z c_i^{\dagger}c_i, \tag{11}$$

where g is the Landé g-factor (typically $g \approx 2$ for electrons), μ_{B} is the Bohr magneton $\mu_{\mathrm{B}} = \frac{e\hbar}{2m_e}$, B is the magnetic field strength, σ_z is the Pauli matrix for spin, $c_i^{\dagger}$ and c_i are the creation and annihilation operators for electrons at site i.

Here, the Landé g-factor is treated as an effective constant parameter within the tight-binding framework, in contrast to momentum-dependent treatments commonly used $\vec{k}\cdot\vec{p}$ in approaches.

Zeeman effect lifts the spin degeneracy, resulting in spin-resolved band splitting. In the absence of a magnetic field, the flat band is typically spin-degenerate (i.e. electrons with spin up and spin down have the same energy). With a magnetic field, the energy levels split into two branches corresponding to spin-up and spin-down electrons(see figure 5). This splitting is linear with the magnetic field strength

$$\begin{aligned} E_{\text{spin-up}} &= E_0 + \frac{1}{2}g\mu_{\mathrm{B}}B, \\ E_{\text{spin-down}} &= E_0 - \frac{1}{2}g\mu_{\mathrm{B}}B, \end{aligned} \tag{12}$$

where E_0 is the energy of the flat band in the absence of the magnetic field. Therefore, the energy-level splitting is given by

$$\Delta E = E_{\text{spin-up}} - E_{\text{spin-down}} = g\mu_{\mathrm{B}}B, \tag{13}$$

which represents the linear form of the Zeeman splitting, valid in the weak magnetic field approximation.

7. High-symmetry points in the Brillouin zone

The band structures are calculated along a standard high-symmetry path in the two-dimensional Brillouin zone of the Lieb lattice. The chosen path is $\Gamma \to X \to M \to \Gamma$, where the high-symmetry points correspond to $\Gamma = (0,0), X = (\pi,0), M = (\pi,\pi)$. These points represent special locations in the reciprocal

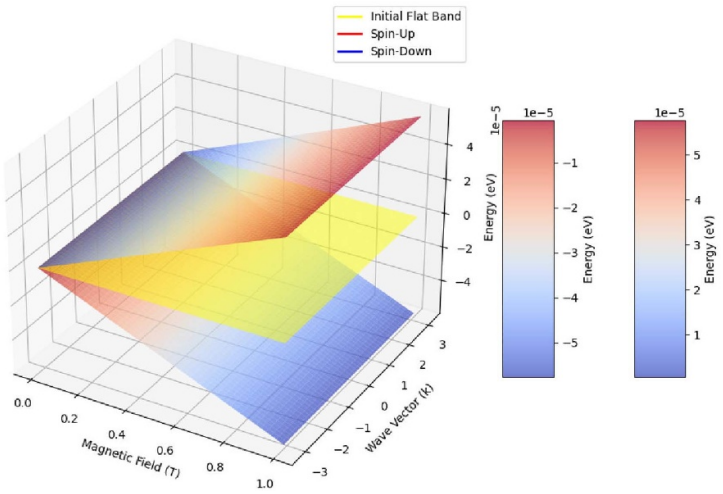

Figure 5. The influence of Zeeman effect on the energy structure of a Lieb lattice in the presence of magnetic field, i.e. the flat band of the energy levels split into two branches corresponding to spin-up $E_{\mathrm{spin-up}}$ and spin-down $E_{\mathrm{spin-down}}$ electrons, respectively.

space that reflect the underlying lattice symmetries and boundary conditions. Calculating the energy bands along this path captures the essential features of the dispersion relations and allows one to identify critical phenomena such as band crossings, gaps, and flat bands. Therefore, this choice of high-symmetry path enables clear and physically meaningful comparisons between different scenarios, such as zero magnetic flux, $\phi = \pi$ flux exhibiting AB caging, and various Zeeman field strengths inducing spin splitting.

The band structures shown in figures 6(a) and (c) are plotted along the high-symmetry path $\Gamma \rightarrow X \rightarrow M \rightarrow \Gamma$ in the two-dimensional Brillouin zone of the Lieb lattice, where $\Gamma = (0,0)$, $X = (\pi,0)$, and $M = (\pi,\pi)$. This path captures the essential features of the lattice's band topology and allows clear visualization of magnetic flux and Zeeman-induced effects.

Figure 6(a) compares the band structures without magnetic flux $\phi = 0$ and with maximal flux $\phi = \pi$. The application of $\phi = \pi$ induces the AB caging effect, leading to perfectly flat energy bands across the Brillouin zone. These flat bands indicate complete localization of wavefunctions due to destructive interference caused by the magnetic phases. The corresponding DOS in figure 6(b) reflects these changes: the flat bands at $\phi = \pi$ produce sharp, delta-function-like peaks, contrasting with the broader DOS at $\phi = 0$. Figures 6(c) and (d) extend the analysis by including Zeeman splitting under various out-of-plane magnetic fields B_z. The spin degeneracy is lifted, doubling the number of bands to six, with clear splitting proportional to B_z. This spin splitting modifies both the band dispersion and the DOS, which gradually evolves from sharp single peaks into multiple spin-polarized peaks, indicating spin-resolved localized states.

Figures 6(a) and (b) show the flattening of the energy bands and the emergence of a prominent zero-energy peak in the DOS at $\phi = \pi$, reflecting the AB caging effect and the corresponding localization of electronic states. In contrast, figures 6(c) and (d) reveal the spin-dependent deformation of bands and splitting of the flat band into spin-polarized subbands as the Zeeman energy B_z increases. This splitting leads to additional fine structure in the DOS, with clear signatures of band separation and spin-resolved flattening.

Lieb lattice provides a paradigmatic platform to study the interplay of magnetic field effects on band topology and localization phenomena. Experimental advances in controlling excited-band lifetimes via lattice-depth optimization [59] highlight the practicality of realizing and probing band deformation effects in optical Lieb lattices. The introduction of a uniform magnetic flux ϕ through the lattice plaquettes induces Peierls phases, modifying the hopping amplitudes and leading to the celebrated AB caging effect at $\phi = \pi$. This effect manifests as complete flattening of energy bands, reflecting perfectly localized eigenstates that cannot propagate due to destructive interference of electron wavefunctions.

Consequently, the combination of Zeeman splitting and AB-induced dispersion can lead to a rich variety of energy level structures. The flat band can split into multiple sub-bands with different dispersions. The energy levels of the flat band can shift upwards or downwards depending on the spin orientation and the specific path taken by the electrons in the lattice. In some cases, the magnetic field can

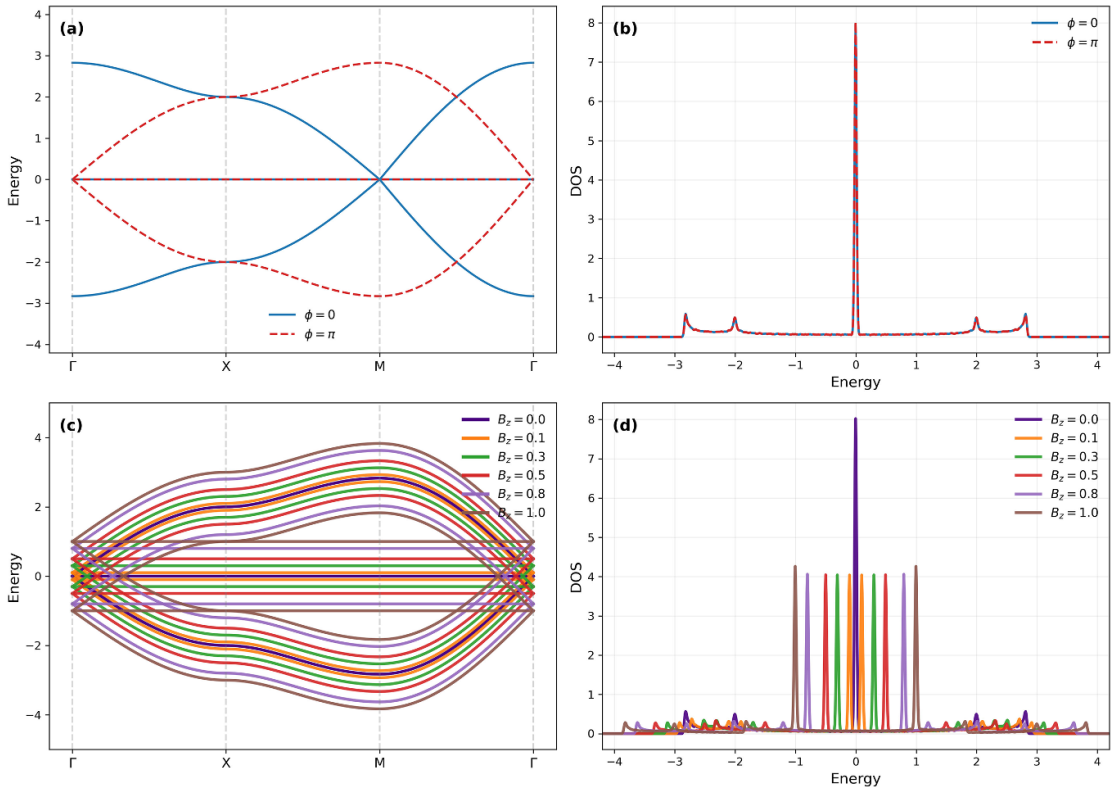

Figure 6. (a) Band structures of the Lieb lattice along the high-symmetry path $\Gamma \to X \to M \to \Gamma$ for magnetic flux $\phi = 0$ (solid blue lines) and $\phi = \pi$ (dashed red lines). The flat bands at $\phi = \pi$ result from the AB caging effect. (b) Corresponding DOS for $\phi = 0$ and $\phi = \pi$, illustrating the emergence of flat bands as sharp peaks in the DOS at $\phi = \pi$. (c) Band structures at $\phi = \pi$ with Zeeman splitting induced by various B_z fields (colors indicate different Zeeman strengths), showing spin-resolved splitting of the previously flat bands into six spin-polarized bands. (d) Corresponding DOS with Zeeman splitting, revealing the gradual splitting and broadening of flat-band peaks with increasing B_z. The high-symmetry points in the Brillouin zone are $\Gamma = (0, 0)$, $X = (\pi, 0)$ and $M = (\pi, \pi)$.

induce transitions between different quantum states, leading to the emergence of new phases or states of matter (e.g. fractional quantum Hall states). These effects highlight the interplay between quantum mechanics and external fields, and they provide a rich playground for exploring novel quantum phenomena in condensed matter systems.

8. Conclusion

In summary, we have explored the magnetic-field-induced band deformation in the Lieb lattice by incorporating both the Peierls substitution and Zeeman splitting. Our calculations reveal a coherent picture in which AB caging and spin-selective Zeeman coupling act in concert to reshape the flat bands, localization, and spin textures. The interplay between magnetic flux and spin splitting thus provides a versatile and controllable means of engineering flatness and magnetic responses in synthetic lattices. By systematically analyzing the evolution of the energy bands, DOS, and spin-resolved structures, we demonstrate that the π-flux condition leads to complete destructive interference and localized flat bands, while the Zeeman term introduces a tunable spin-resolved deformation of these bands. This dual control mechanism bridges magnetic interference and spin physics within a unified framework and highlights the spin-selective nature of AB caging.The inclusion of weak interaction effects constitutes a natural and experimentally relevant extension of the present work, and may enable the exploration of correlated and nonequilibrium phenomena in flat-band systems under synthetic magnetic fields.

Recent experimental advances in engineered lattice systems provide a timely and realistic context for our theoretical results. Magnetic-field-induced band deformation, flat-band localization, and spin-resolved control have been experimentally demonstrated across a range of platforms, including ultracold atoms with synthetic gauge fields [60, 61], photonic Lieb and flat-band lattices [62, 63], and engineered synthetic lattices such as superconducting, microwave, and Rydberg-atom systems [64, 65]. In particular, the realization of artificial magnetic flux and controllable band engineering in ultracold atoms, together with observations of flat-band localization in photonic and driven-dissipative lattices, highlights the

experimental accessibility of the interference-driven mechanisms discussed here. Recent Rydberg-atom synthetic lattice experiments further extend these ideas toward regimes where interactions and nonequilibrium effects become important. These developments place our work within a rapidly evolving experimental landscape and underscore its relevance to ongoing and future studies of flat-band physics under synthetic magnetic fields.

With the rapid progress of quantum simulation techniques, the Lieb lattice has emerged as a promising platform to experimentally probe such field-driven phenomena. The tunability of ultracold atoms, photonic lattices, and circuit-QED arrays enables the realization of synthetic magnetic fields and controllable spin degrees of freedom. Our study therefore provides both conceptual and quantitative guidance for flat-band engineering and spin-controlled localization, offering insight for future exploration of correlated and topological phases in designer lattice geometries.

Acknowledgments

This work is supported by the National Natural Science Foundation of China (Grants no. 92365208) and National Key Research and Development Program of China (Grants no. 2021YFA0718300 and no. 2021YFA1400900).

Data availability statement

All data that support the findings of this study are included within the article (and any supplementary files).

ORCID iDs

Nana Chang 0000-0003-3631-4426
Xiaoji Zhou 0000-0001-9175-2854

References

[1] Taie S, Ozawa H, Ichinose T, Nishio T, Nakajima S and Takahashi Y 2015 *Sci. Adv.* **1** e1500854
[2] Mukherjee S, Di Liberto M, Öhberg P, Thomson R R and Goldman N 2018 *Phys. Rev. Lett.* **121** 075502
[3] Jiang J, Gao Y, Li L, Liu Y, Zhu W, Zhu C, Francisco J S and Zeng X C 2024 *Nat. Phys.* **20** 456–62
[4] Bello M, Arze S and Greschner S 2019 *New J. Phys.* **21** 033050
[5] Tang E, Mei J W and Wen X G 2011 *Phys. Rev. Lett.* **106** 236802
[6] Neupert T, Santos L, Chamon C and Mudry C 2011 *Phys. Rev. Lett.* **106** 236804
[7] Leykam D, Andreanov A and Flach S 2018 *Adv. Phys. X* **3** 1473052
[8] Chen Y, Huang J, Jiang K and Hu J 2023 *Sci. Bull.* **68** 3165–71
[9] Chang N, Gundogdu S, Leykam D, Angelakis D G, Kou S, Flach S and Maluckov A 2021 *APL Photonics* **6** 030801
[10] Leykam D, Flach S, Bahat-Treidel O and Desyatnikov A S 2013 *Phys. Rev. B* **88** 224203
[11] Flach S, Leykam D, Bodyfelt J D, Matthies P and Desyatnikov A S 2014 *Europhys. Lett.* **105** 30001
[12] Mallick A, Chang N, Andreanov A and Flach S 2022 *Phys. Rev. A* **105** L021305
[13] Mallick A, Chang N, Maimaiti W, Flach S and Andreanov A 2021 *Phys. Rev. Res.* **3** 013174
[14] Ozawa T *et al* 2019 *Rev. Mod. Phys.* **91** 015006
[15] Gross C and Bloch I 2017 *Science* **357** 995–1001
[16] Vicencio R A, Cantillano C, Morales-Inostroza L, Real B, Mejía-Cortés C, Weimann S, Szameit A and Molina M I 2015 *Phys. Rev. Lett.* **114** 245503
[17] Whittaker C E, Gulevich D R, Biegańska D, Royall B, Clarke E, Skolnick M S, Shelykh I A and Krizhanovskii D N 2021 *Phys. Rev. A* **104** 063505
[18] Lieb E H 1989 *Phys. Rev. Lett.* **62** 1201–4
[19] Weeks C and Franz M 2010 *Phys. Rev. B* **82** 085310
[20] Shen R, Shao L B, Wang B and Xing D Y 2010 *Phys. Rev. B* **81** 041410
[21] Goldman N, Urban D F and Bercioux D 2011 *Phys. Rev. A* **83** 063601
[22] Apaja V, Hyrkäs M and Manninen M 2010 *Phys. Rev. A* **82** 041402
[23] Mukherjee S, Spracklen A, Choudhury D, Goldman N, Öhberg P, Andersson E and Thomson R R 2015 *Phys. Rev. Lett.* **114** 245504
[24] Mukherjee S and Thomson R R 2017 *Opt. Lett.* **42** 2243–6
[25] Yin G, Lai C K, Chang N, Liang Y, Mao D and Zhou X 2024 *Front. Phys.* **19** 62201
[26] Li L and Others 2022 *Nat. Phys.* **18** 1124–9
[27] Parto M, Mukherjee S, Plasencia M, Piper K, Leykam D, Mejía-Cortés C, Guzmán-Silva D, Thomson R R, Szameit A and Goldman N 2019 *Nat. Phys.* **15** 1100–5
[28] Vidal J, Douçot B, Mosseri R and Butaud P 2000 *Phys. Rev. Lett.* **85** 3906–9
[29] Mukherjee S, Parto M and Goldman N 2020 *Nat. Phys.* **16** 818–23
[30] Vidal J, Mosseri R and Douçot B 1998 *Phys. Rev. Lett.* **81** 5888–91
[31] Nicolau E, Marques A M, Dias R G, Mompart J and Ahufinger V 2023 *Phys. Rev. A* **107** 023305
[32] Guzmán-Silva D, Mejía-Cortés C, Bandres M A, Rechtsman M C, Weimann S, Nolte S, Segev M, Szameit A and Vicencio R A 2014 *New J. Phys.* **16** 063061
[33] Roushan P *et al* 2017 *Nat. Phys.* **13** 146–51

[34] Lorentz H A 1897 Attempt of a theory of electrical and optical phenomena in moving bodies
[35] Demtröder W 2014 *Atoms, Molecules and Photons* (Springer) (available at: www.springer.com/gp/book/9783662462171)
[36] Zeeman P 1897 *Phil. Mag.* **43** 226–39
[37] Born M and Wolf E 1999 *Principles of Optics* 7th edn (Cambridge University Press)
[38] Sakurai J J and Napolitano J 2020 *Modern Quantum Mechanics* 3rd edn (Cambridge University Press) https://doi.org/10.1017/9781108587280
[39] Griffiths D J 2017 *Introduction to Quantum Mechanics* 3rd edn (Cambridge University Press) https://doi.org/10.1017/9781316995433
[40] Foot C J 2004 *Atomic Physics* (Oxford University Press) https://doi.org/10.1093/oso/9780198506959.001.0001
[41] Feynman R P, Leighton R B and Sands M 1963 *The Feynman Lectures on Physics III* (Addison-Wesley)
[42] Wirth G, Ölschläger M and Hemmerich A 2011 *Nat. Phys.* **7** 147–53
[43] Jo G B, Guzman J, Thomas C K, Hosur P, Vishwanath A and Stamper-Kurn D M 2012 *Phys. Rev. Lett.* **108** 045305
[44] Nascimbène Y, Chen Y A, Atala M, Aidelsburger M, Trotzky S, Paredes B and Bloch I 2013 *Phys. Rev. Lett.* **110** 205301
[45] Windpassinger P and Sengstock K 2013 *Rep. Prog. Phys.* **76** 086401
[46] Chang N N and Xue J K 2018 *Chin. Phys. B* **27** 105203
[47] Chang N N, Jing W Q, Zhang Y, Zhang A X, Xue J K and Kou S P 2020 *Chin. Phys. B* **29** 010306
[48] Aidelsburger M, Atala M, Lohse M, Barreiro J T, Paredes B and Bloch I 2013 *Phys. Rev. Lett.* **111** 185301
[49] Miyake H, Siviloglou G A, Kennedy C J, Burton W C and Ketterle W 2013 *Phys. Rev. Lett.* **111** 185302
[50] Jotzu G, Messer M, Desbuquois R, Lebrat M, Uehlinger T, Greif D and Esslinger T 2014 *Nature* **515** 237–40
[51] Goldman N, Juzeliūnas G, Öhberg P and Spielman I B 2016 *Rep. Prog. Phys.* **77** 126401
[52] Goldman N and Dalibard J 2014 *Phys. Rev. X* **4** 031027
[53] Slot M R, Gardenier T S, Jacobse P H, Van Miert G C P, Kempkes S N, Zevenhuizen S J M, Smith C M, Vanmaekelbergh D and Swart I 2017 *Nat. Phys.* **13** 672–6
[54] Drost R, Ojanen T, Harju A and Liljeroth P 2017 *Nat. Phys.* **13** 668–71
[55] Wu S, Xu C, Wang X, Lin H Q, Cao C and Cao G H 2025 *Nat. Commun.* **16** 1375
[56] Yang J, Li Y, Yang Y, Xie X, Zhang Z, Yuan J, Cai H, Wang D W and Gao F 2024 *Nat. Commun.* **15** 1484
[57] Taie S, Ichinose T, Ozawa H and Takahashi Y 2020 *Nat. Commun.* **11** 257
[58] Zohuri B 2024 *J. Energy Power Eng.* **18** 79–87
[59] Shui H, Lai C K, Yu Z, Tian J, Wu C, Chen X and Zhou X 2023 *Opt. Express* **31** 26599–609
[60] Aidelsburger M *et al* 2020 *Nat. Phys.* **16** 441–6
[61] Tai M 2022 *Phys. Rev. Lett.* **129** 220403
[62] Vicencio R A *et al* 2015 *Phys. Rev. Lett.* **114** 245504
[63] Mukherjee S *et al* 2025 *Commun. Phys.* **8** 138
[64] Weimer H *et al* 2024 *Phys. Rev. Res.* **6** 013045
[65] Semeghini G *et al* 2025 *Nat. Phys.* **21** 221–7